ROYAL SOCIETY OF CHEMISTRY

PAPER

Check for updates

Unveiling the sensing ability of new MoS$_2$ nanoparticles: from fundamental insights into practical applications for nitrites†

Federica Florio,[a] Angelo Ferlazzo, [iD][a] Stefano Bonforte,[a] Giuseppe Nicotra,[b] Giovanni Neri, [iD][c] Iddo Pinkas, [iD][d] Milko E. van der Boom [iD] *[e] and Antonino Gulino [iD] *[a]

The unique properties of transition metal dichalcogenides (TMDs), particularly molybdenum disulfide (MoS$_2$), have garnered significant attention in various fields including electronics, catalysis, and energy storage. The synthesis of MoS$_2$, along with controlled morphology and properties, remains a crucial aspect because of its practical applications. Here, we present an alternative synthesis approach for MoS$_2$, obtained by a solvothermal method, starting from bis(acetylacetonato)dioxomolybdenum(VI), MoO$_2$(acac)$_2$. Our method results in the formation of a carbon MoS$_2$ ($\sim$75% : $\sim$25%) composite material. This composite holds promise for advancing our understanding and utilization of MoS$_2$ for sensing. Through detailed characterization and analysis, we elucidate the structure and morphology of the synthesized MoS$_2$, and provide insights into its sensing applications for nitrites. This study not only contributes to the synthesis methodology of MoS$_2$—it also offers valuable insights for the design and development of advanced TMD-based materials.

[a] Department of Chemical Sciences, University of Catania, and I.N.S.T.M. U.d.R. of Catania, Viale Andrea Doria 6, 95125 Catania, Italy. E-mail: antonino.gulino@unict.it

[b] CNR-IMM, Z.I. VIII Strada 5, Catania, 95121, Italy

[c] Department of Engineering, University of Messina, Contrada Di Dio, 98166 Messina, Italy

[d] Chemical Research Support, Weizmann Institute of Science, Rehovot 7610001, Israel

[e] Department of Molecular Chemistry and Materials Science, Weizmann Institute of Science, Rehovot 7610001, Israel

† Electronic supplementary information (ESI) available: Table S1 optimized reaction method and conditions; Fig. S1 XRD pattern of the synthesized MoS$_2$/C composite; Fig. S2 EELS spectrum of the MoS$_2$/C composite; Fig. S3(a) electrochemical behavior of SPCE, and MoS$_2$/SPCE; (b) cyclic voltammogram of SPCE and MoS$_2$/SPCE in the presence of 10 mM K$_3$[Fe(CN)$_6$]; (c) EIS of SPCE and MoS$_2$/SPCE; (d) cyclic voltammogram of MoS$_2$/SPCE in the presence of 10 mM K$_3$[Fe(CN)$_6$] at different scan rates; Fig. S4 (a) Electrochemical behavior (0–1 V potential range, in PBS) of: SPCE (black dotted line) and MoS$_2$/SPCE (red dotted line), SPCE (black solid line) and MoS$_2$/SPCE (red solid line) in the presence of both PBS and 200 μM of NaNO$_2$; (b) comparison between the responses of SPCE and MoS$_2$/SPCE in the presence of 200 μM of NaNO$_2$; Fig. S5(a) LSV of MoS$_2$/SPCE at different nitrite concentrations; (b) graph of the anodic peak current (I_{pa}) *versus* the NO$_2^-$ concentration; Fig. S6(a) repeatability of the performance of MoS$_2$/SPCE; (b) DPV analyses to determine NaNO$_2$ in a real sample; (c) DPV analyses at t = 0, and at [t = 6 months]; Fig. S7 DPV analyses a different pH (5.0, 6.0, 7.4, 8.0); Fig. S8 DPV analyses in PBS 0.1 M, and PBS 0.1 M and NaCl 0.1 M. See DOI: https://doi.org/10.1039/d5tc01165e

Introduction

Transition metal dichalcogenides (TMDs) are a set of MX$_2$ inorganic compounds, where M belongs to the IV–IX groups, and X is a chalcogen ion (S, Se, Te).[1,2] Depending on the number of d-electrons of M and on the X oxidation state, TMDs can be insulators, semiconductors, or metallic.[3] Within TMDs, MoS$_2$ exhibits unique properties that mainly develop from its layered structure.[4] Therefore, bulk and monolayer MoS$_2$ exhibits an indirect bandgap of $\sim$1.2 eV or a direct bandgap of $\sim$1.8 eV, respectively.[5,6] MoS$_2$ undergoes the following three main crystalline phases: 1T (one-layered trigonal, metallic), 2H (two-layered hexagonal, semiconductor), and 3R (three-layered rhombohedral, semiconductor), where 1, 2, and 3 indicate the number of MoS$_2$ layers contained in the unit cell, and the letters T, H, and R refer to the lattice systems.[7,8]

MoS$_2$ has recently emerged as a promising material for sensing applications due to its unique electronic, mechanical, and chemical properties.[9,10] The layered structure of MoS$_2$, along with its high surface-to-volume ratio and tunable bandgap, makes it an attractive candidate for sensing platforms.[11] Considerable research efforts have been directed toward exploring and harnessing the sensing capabilities of MoS$_2$ in environmental monitoring, healthcare diagnostics, and industrial process control.[12–14] In this context, the sensing of widely used nitrites as additives in the food industry is important, since, within the human body, nitrites can easily be transformed into nitrosamines. Importantly, these compounds are a probable human carcinogen.[15,16] Typical sensing approaches for nitrites involve Raman spectroscopy, chromatography, spectrophotometry,

chemiluminescence, supramolecular receptors, and electrochemical measurements.[17–19] Electrochemical methods offer a combination of practical advantages regarding sensitivity, selectivity, and possible miniaturization.[20] Nanostructured MoS_2-based sensors are responsive toward NO_2^-. Zhang *et al.* used a flower-like 3D MoS_2 microsphere/2D C_3N_4 nanosheet composite for the electrochemical sensing of nitrite and found a large and linear detection range (0.1–1100 μM), and a detection limit of 0.065 μM.[21] Li *et al.* used high-valence Mo(vi) derived from *in situ*-oxidized MoS_2 nanosheets for nitrite sensing and reported a linear relationship with nitrite concentrations ranging from 1.0 μM to 386.0 μM with an even lower detection limit of 0.028 μM.[22] Ghanei-Motlagh used a silver/halloysite nanotube/molybdenum disulfide nanocomposite for nitrite sensing and observed a linear response from 2 to 425 μM with a detection limit of 0.7 μM.[23]

Nanostructured MoS_2 can be synthesized by both bottom-up and top-down approaches.[24] We have chosen, among the bottom-up approaches, the solvothermal method that embodies the best compromise between a straightforward synthesis procedure and the desirable properties of the final product.[25] In this study, we demonstrated the use of the commercially available $MoO_2(acac)_2$ as a precursor for the formation of a composite of MoS_2/C and the detection of nitrites. We focused on the electrochemical behavior of this composite to systematically investigate its sensing performance and elucidate its response mechanism. Through comprehensive characterization and analyses, we provide insights into its suitability for practical sensing applications. The detection limit of the composite toward nitrite ions is appreciably below the permissible limit in potable water. We also demonstrate its use for detecting nitrite ions in a meat product.

Experimental

Some chemicals were of reagent grade and were used without further purification. The following compounds were purchased from Sigma Aldrich: bis(acetylacetonato)dioxomolybdenum, $MoO_2(acac)_2$ was purified by multiple sublimation procedures at 120 °C under vacuum,[26] sulfur, 1-methyl-2-pyrrolidone (NMP), purity ≥99.0%.

MoS_2 synthesis

1.0770 g (3.302 mmol) of $MoO_2(acac)_2$ and 0.318 g (9.906 mmol) of sulfur were dissolved in 60 mL of NMP with two drops of water. Then, the mixture was stirred for 30 minutes, transferred into a 100 mL Teflon-lined stainless steel autoclave and heated at 200 °C for 24 h. Next, the autoclave was left to cool down to room temperature and a black precipitate was collected by centrifugation (14 000 rpm) and washed with NMP, ethanol, and water. Finally, the product was dried in a vacuum oven at 60 °C for 24 h; the yield = 0.528 g of overall product (0.396 g C, 0.132 g MoS_2), 25% with respect to MoS_2.

X-ray photoelectron spectroscopy (XPS)

These measurements were made at a 45° take-off angle relative to the surface normal using a PHI 5000 Versa Probe II system (ULVAC-PHI, Inc.). The base pressure of the main chamber was 1×10^{-8} Pa. Samples were excited with monochromatized Al K_α X-ray radiation using a pass energy of 5.85 eV. Spectra were calibrated by fixing the Ag $3d_{5/2}$ peak of a clean sample at 368.3 eV. The instrumental energy resolution was ≤0.5 eV. The XPS peak intensities were obtained after Shirley background removal. The atomic concentration was analyzed by considering the relevant atomic sensitivity factors. The fittings of the Mo 3d, S 2s, S 2p, XP spectra were carried out with the XPSPEAK4.1 software using Gaussian envelopes after subtracting the background until there was the highest possible correlation between the experimental spectra and the theoretical profiles. The residual or agreement factor R was defined as $R = \left[\sum (F_{obs} - F_{calc})^2 \Big/ \sum (F_{obs})^2 \right]^{1/2}$, after minimizing the function $\sum (F_{obs} - F_{calc})^2$, which converged to a value of 0.03.[27–29]

X-Ray diffraction (XRD)

A Rigaku Smartlab diffractometer was used, equipped with a rotating anode of Cu K_α radiation, operating at 45 kV and 200 mA. Bragg–Brentano patterns were acquired with a resolution step of 0.02° 2θ.

Raman measurements

The micro-Raman spectra (λ = 532 nm excitation laser) were collected using a Horiba LabRAM HR Evolution (Horiba, France) spectrometer equipped with four laser lines (785, 633, 532, and 325 nm). The system has an 800 mm focal length spectrograph for high-resolution and low stray light, with several interchangeable gratings; it includes an open electrode, front illuminated, cooled CCD detector. The sample was placed under a modular microscope (Olympus BX-FM) with a suitable objective. For this work, a MPlanFL N × 150 NA = 0.9 BD (Olympus Japan) objective with spatial resolution better than 1 μm was used. The Raman scattered light from the sample was dispersed by a 600 g mm^{-1} grating and the pixel resolution was better than 2 cm^{-1}. Spectra were collected between 100 and 1800 cm^{-1}, with a power of up to 3 mW, and an exposure of 20–100 seconds using 5–20 averages (depending on the signal quality). The system was calibrated using the Si peak at 520.7 cm^{-1} before every measurement session.

Electron microscopy

Scanning electron microscopy (SEM) images were acquired using an Everhart–Thornley detector installed on a Thermo Scientific™ Helios™ 5 UC DualBeam system, equipped with a monochromated SFEG electron gun, operating at 5.00 kV. A JEOL ARM 200F electron microscope was used to characterize the MoS_2/C composite by scanning transmission electron microscopy in high annular angle dark field mode (HRSTEM-HAADF) and electron energy-loss spectroscopy (EELS) analyses. Measurements were conducted under gentle STEM conditions

This journal is © The Royal Society of Chemistry 2025

J. Mater. Chem. C, 2025, **13**, 11214–11222 | **11215**

(60 keV, a probe size of 1.1 Å, and 5 μA emission current) to prevent the sample from beam damage.[30]
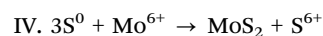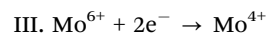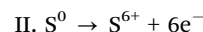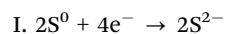
Electrochemistry

Cyclovoltammetry (CV), linear sweep voltammetry (LSV), and differential pulse voltammetry (DPV) measurements were performed using a DropSens μStat 400 potentiostat equipped with Dropview 8400 software. Electrical impedance spectroscopy (EIS) was performed using a Metrohm Autolab galvanostatic potentiostat. A 0.1 M phosphate buffered saline (PBS) solution at pH 7.4 was used to perform the electrochemical measurements. CV tests were performed at a scan rate of 50 mV s^{-1} in the −0.3 to 0.6 V potential range, using 10 mM potassium ferricyanide ($K_3[Fe(CN)_6]$) and 0.1 M KCl standard solutions. LSV tests were conducted using a 0.1 M PBS solution, at a scan rate of 50 mV s^{-1}, in a 0–1 V potential range, to detect 0–1000 μM $NaNO_2$ concentrations, with steps of 10 μM. DPV tests were conducted using an optimized potential step (E_{step}) of 0.03 V, a potential pulse (E_{puls}) of 0.09 V, and a time pulse (T_{pul}) of 200 ms with a scan rate of 40 mV s^{-1}. EIS tests were conducted using 10 mM potassium ferricyanide ($K_3[Fe(CN)_6]$) and 0.1 M KCl standard solutions in the 0.1–105 Hz frequency range, an amplitude of 5 mV, and an applied potential of 0.25 V. Measurements were made using commercial screen-printed electrodes, with a carbon working electrode (SPCE) from Methrom DropSens company; the SPCE was modified with MoS_2/C composite (hereafter referred to as MoS_2/SPCE). This sensor was prepared by depositing 20 μL of a suspension of the MoS_2/C composite (1 mg in 1 mL of distilled water) on the working electrode. The resulting sensor was air-dried at room temperature for 24 hours. The sensor's sensitivity was always calculated as the ratio between the slope of the calibration line and the geometric surface area of the used electrode (0.125 cm^2).[31] The limit of detection (LOD) was calculated by multiplying the ratio between the intercept value and the slope of the calibration line by 3.3. Chronoamperometric curves were obtained by recording the oxidation current, under a constant potential of 0.6 V, while an appropriate volume of 10 mM of the NO_2^- solution was added to the electrolyte solution (PBS 0.1 M) under magnetic stirring.

DPV nitrite sensing measures were also performed at different pH (5–8) and ionic strength (0.1 M, 0.2 M) values.
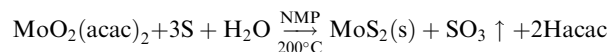
To assess the ability of the MoS_2/SPCE sensor to detect NO_2^- anions in a real water sample, we performed the DPV analysis on commercial bottled water (Fontenoce; its physico-chemical analysis indicated the absence of nitrite anions) before and after adding 1, 2, and 20 μM of nitrite anion, respectively. The MoS_2/SPCE can be reset by washing with distilled water. In addition, we investigated the nitrite concentration in an Italian sausage (bresaola punta d'anca RIGAMONTI; https://www.rigamontisalumificio.it) by DPV using the already optimized potential step, potential pulse, time pulse, and scan rate. Next, we minced a bresaola slice of 10.1 g using a Beku blender in 100 mL of water and after 2 h, we filtered off the liquid. Finally, we diluted 1 mL of this liquid to 5 mL using 4 mL of distilled water and measured the resulting solution.

Results and discussion

Concerning the solvothermal syntheses of MoS_2, it was reported that varying the reaction temperature, from 180 °C to 240 °C, results in different degrees of crystallinity and structures, along with a great variety of morphologies (e.g., nanorods, nanosheets, and nanospheres).[32] In our solvothermal process we used $MoO_2(acac)_2$ as a metal–organic precursor. A possible reaction mechanism for the MoS_2 formation involves a redox process in which Mo(VI) is reduced to Mo(IV) and sulfur is involved in a disproportion reaction:

$$\text{I. } 2S^0 + 4e^- \rightarrow 2S^{2-}$$

$$\text{II. } S^0 \rightarrow S^{6+} + 6e^-$$

$$\text{III. } Mo^{6+} + 2e^- \rightarrow Mo^{4+}$$

$$\text{IV. } 3S^0 + Mo^{6+} \rightarrow MoS_2 + S^{6+}$$

Overall reaction:

$$MoO_2(acac)_2 + 3S + H_2O \xrightarrow[200°C]{NMP} MoS_2(s) + SO_3 \uparrow + 2Hacac$$

The graphitic carbon was produced by decomposing Hacac.[33]

Another key factor in our synthetic method is the choice of NMP as solvent. The surface tension value of 40 mJ m^{-2} matches the surface energy estimated for few-layered MoS_2, namely, 46.5 mJ m^{-2}.[34] NMP is often used to exfoliate layered materials and to stabilize the thin sheets, produced by material ultrasonication, after the synthesis.[34] However, such a procedure may induce undesired oxidation processes and consequently the formation of undesired sulfur vacancies.[35] Taking all this into account, we employed NMP as the solvent for the MoS_2/C syntheses to obtain a layered nanostructure without further post-synthetic treatment. The other important parameter in our solvothermal synthesis is the temperature, which was set at a value (200 °C) close to the boiling point of NMP (202 °C).

Fig. 1a presents a comprehensive micro-Raman spectrum of the MoS_2/C composite in the 100–1800 cm^{-1} range, and Fig. 1b provides the 100–500 cm^{-1} region.

The peaks observed at 150, 239, 285, and 337 cm^{-1} correspond to the characteristic J_1, J_2, E_{1g}, and J_3 MoS_2 vibrational modes, respectively, which were indicative of the 1T-phase of MoS_2.[36] On the other hand, the peaks at 376 and 405 cm^{-1} correspond to the E_{2g}^1 and A_{1g} vibrational modes of the 2H-phase of MoS_2, respectively.[3,37] In addition, the peaks at 113 and 125 cm^{-1} correspond to the B_{1g} and B_{2g} vibrational modes associated with some MoO_3 compounds, as well as the peaks at 660, 820, 964, and 993 cm^{-1}.[36,38,39] The vibrational modes at 1378 and 1562 cm^{-1} correspond to the D and G bands of graphitic carbon, respectively.[40] Therefore, the Raman data confirm the presence of a composite material consisting of graphitic carbon as well as the MoS_2 1T and 2H mixed phases.
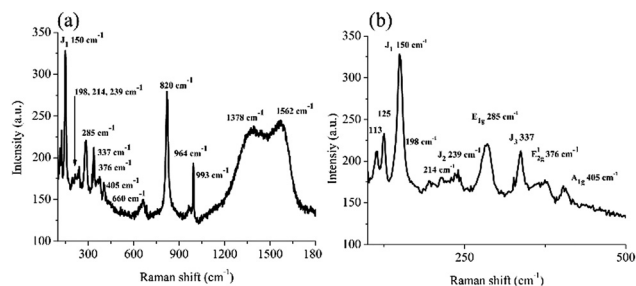
11216 | *J. Mater. Chem. C*, 2025, **13**, 11214–11222

This journal is © The Royal Society of Chemistry 2025

Paper

Fig. 1 (a) Micro-Raman spectrum of the MoS$_2$/C composite in the 100–1800 cm^{-1} range. The low frequency shows MoO$_3$ and MoS$_2$; the middle frequencies show other oxides, and the higher frequencies belong to the carbonaceous material; (b) an expanded scale in the 100–500 cm^{-1} range shows the assignments of the MoS$_2$ vibrations (1T and 2H) and the MoO$_3$ oxide.

XPS was performed on the as-synthesized MoS$_2$/C to obtain important information about its electronic structure. Fig. 2a shows the XP spectrum of the Mo 3d and S 2s states. Three peaks were evident at 226.5, 229.1, and 232.3 eV. Deconvolution of the experimental XP spectrum revealed the presence of a band at 226.5 eV due to the S 2s states. The following six Gaussians correspond to three Mo 3d doublets (Mo 3d$_{5/2,3/2}$ spin–orbit components). Those Gaussians at 229.0–232.2 eV are consistent with the Mo^{4+} states of the 1T MoS$_2$ phase (39% of the overall Mo content); those at 230.1–233.3 eV are consistent with the Mo^{4+} states of the 2H MoS$_2$ phase (56% of the overall Mo content), and those at 232.2–235.2 eV are consistent with a few Mo^{6+}, due to the presence of some sizeable ($\sim$5% with respect to the total Mo content) MoO$_3$.[26,41–43] The data are in good agreement with the literature regarding layered structured MoS$_2$.[44]

Fig. 2b shows the XP spectrum of the S 2p states. The spectrum revealed two evident peaks and an additional high binding energy shoulder at 162.1, 162.9, and 164.4 eV. Fitting the spectrum
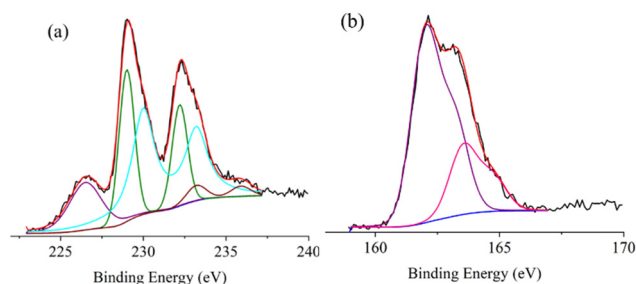
profile disclosed the superimposition of two S 2p$_{3/2,1/2}$ doublets at 162.0–163.2 and 163.5–164.7 eV (1.2 eV spin–orbit coupling), whose single doublet components overlapped. According to the reported results, the lower binding energy doublet refers to both the terminal S$_2^{2-}$ and S^{2-} basal plane ions, whereas the higher binding energy doublet is due to apical S^{2-} and bridging S$_2^{2-}$ ions.[45]

The SEM analysis of MoS$_2$/C reveals granular structures that are highly dispersed in size, irregularly faceted, and with rounded surfaces. These features indicate the absence of well-defined crystallinity and the presence of large grains (Fig. 3).

HRSTEM-HAADF imaging of the MoS$_2$/C composite (Fig. 4a–c) revealed a nanostructured specimen made by a randomly oriented nanoribbon-like matrix very visible in the thinner regions.[46] Layered structures are visible with an average length of 2.79 nm, and typical interplanar distances of 0.60 and 0.90 nm, consistently with the 2H and 1T-MoS$_2$ phases, respectively, which coincide with the Raman analysis.[36]

Both the XRD spectra and the SAED patterns obtained from HRSTEM show broadened diffraction peaks and continuous rings, respectively, which are characteristics of partially ordered crystals with a short-range order of <10 nm for which one observes relevant peak broadening due to a small crystal size.

From the SEM and TEM analyses, it emerges that these nanostructures have a matrix with an intermediate structure between amorphous and crystalline. There are locally ordered regions that exhibit a layered structure with nanoribbon-like morphologies.

Fig. S1 (ESI†) shows the XRD pattern of the MoS$_2$/C composite. As shown, apart from a broad band covering the 30–60 2θ range, no well-defined peaks were observed throughout the 2θ range. This observation reinforces the absence of a long-range order or a defined interlayer spacing. Such a pattern characterizes nanostructures with dimensions well below 10 nm, which lack a long-range order yet retain short-range periodicity.[47] This observation is in good agreement with literature XRD data for a similar nanosized, destacked MoS$_2$ material.[35,48,49] Raman spectroscopy is highly sensitive to local atomic arrangements, allowing the detection of localized phonon modes even under conditions where XRD shows no long-range order.[50] Indeed, the
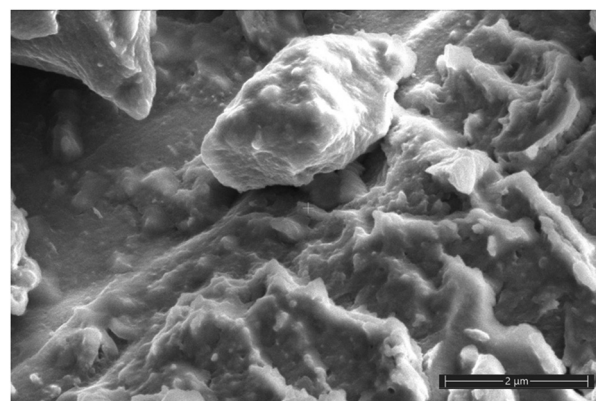

Fig. 2 (a) Al-K$_\alpha$ excited XPS of MoS$_2$ in the Mo 3d$_{5/2,3/2}$, S 2s binding energy region. The olive, cyan, and wine lines denote the 229.0–232.2, 230.1–233.3, and 232.2–235.2 eV components, respectively, of the Mo 3d states, and the purple line denotes the S 2s signal at 226.5 eV. The blue line denotes the background, and the red line superimposed on the experimental black profile denotes the sum of all components. (b) Al-K$_\alpha$ excited XPS of MoS$_2$ in the S 2p$_{3/2,1/2}$ binding energy region. The purple and the pink lines denote the 162.0–163.2 and 163.5–164.7 eV components, respectively, of the S 2p states. The blue line denotes the background, and the red line superimposed on the experimental black profile denotes the sum of all components.

Fig. 3 SEM images of the MoS$_2$/C composite.

This journal is © The Royal Society of Chemistry 2025

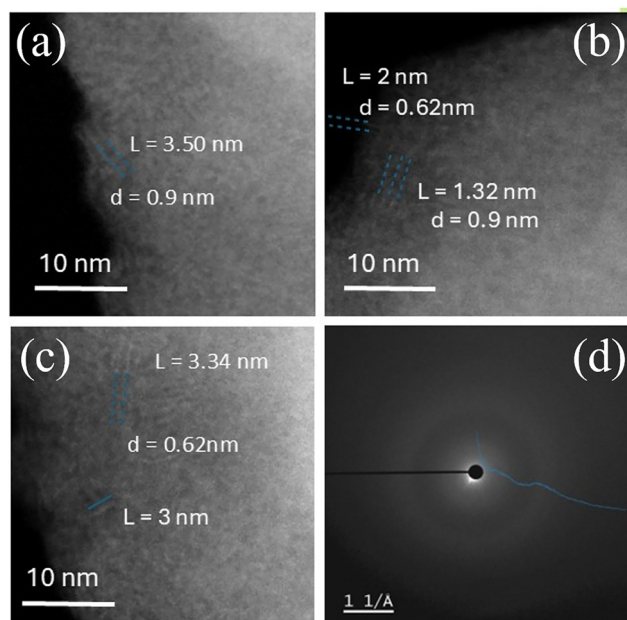J. Mater. Chem. C, 2025, **13**, 11214–11222 | **11217**

Fig. 4 HRSTEM-HAADF images of the MoS$_2$/C composite showing (a) some nanoribbons of 3.50 nm at 0.90 nm; (b) some nanoribbons of 2.00 and 1.32 nm at 0.60 and 0.90 nm, respectively; (c) nanoribbons of 3.00 and 3.34 nm (d = 0.6 nm); (d) a selected area electron diffraction (SAED) pattern and its intensity profile (the cyan line) of the MoS$_2$/C composite.

SAED pattern (Fig. 4d) and the corresponding intensity profile (the cyan line in Fig. 4d), which is in close agreement with the XRD profile (Fig. S1, ESI†), exhibited a "poor crystalline" diffraction signature with blurry halo rings.[4,51]

The EELS spectrum (Fig. S2, ESI†) confirmed that MoS$_2$ is homogeneously dispersed within the carbon matrix.

The electrochemical properties of the MoS$_2$/C composite indicated a band gap of 1.68 eV, estimated from the difference between the LUMO (-4.077 eV) and HOMO (-5.757 eV) energy levels.[52] These HOMO–LUMO levels were calculated from the oxidation and reduction onset from the cyclic voltammogram shown in Fig. 5 using eqn (1) and (2):

$$\text{HOMO} = -[E_{\text{onset,ox}} + 4.637 \text{ eV}] \quad (1)$$

$$\text{LUMO} = -[E_{\text{onset,red}} + 4.637 \text{ eV}] \quad (2)$$

Fig. S3–S5 (ESI†) show the characterization of the MoS$_2$/C composite/SPCE electrode. We performed DPV measurements with the MoS$_2$/SPCE sensor using increasing NO$_2^-$ concentrations (Fig. 6a). Fig. 6b shows the calibration curve of the MoS$_2$/SPCE sensor; it exhibits excellent responsiveness to nitrite concentrations, showing a sensitivity of 4.993 µA µM^{-1} cm^{-2}.[53]

The reported oxidative peak potential of MoS$_2$ is 1.3 V.[5,6] In our carbon MoS$_2$ composite we observed this oxidative peak at 1.6 V.

The Food and Drug Administration (FDA) states that the nitrite anion concentration in water must be lower than 1.0 mg L^{-1} (20 µM); however, we succeeded in detecting much lower concentrations (0.085 µM). Concerning the sensing mechanism for nitrite
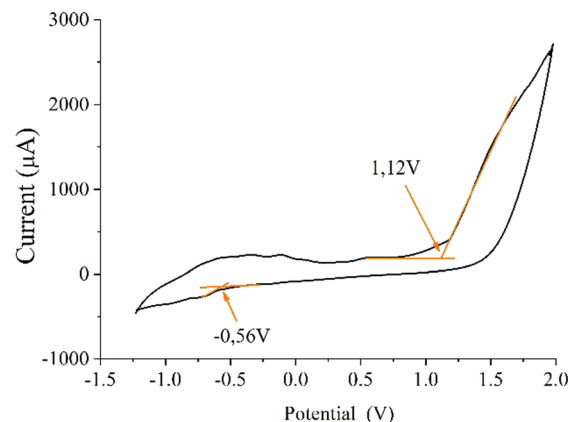

Fig. 5 Cyclic voltammogram *versus* the Ag/AgCl reference electrode of the synthesized MoS$_2$/C composite. The ΔV of the standard hydrogen electrode (SHE) *vs.* vacuum = 4.440 V; the ΔV of the Ag/AgCl *vs.* SHE = 0.197 V; the ΔV of the Ag/AgCl *vs.* vacuum = 4.637 V.
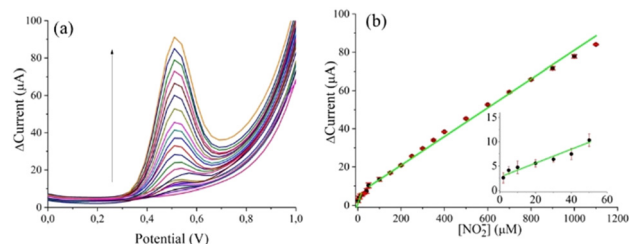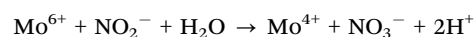

Fig. 6 (a) DPV at different nitrite concentrations (0–1100 µM, initial step 1 µM) in 0.1 M PBS (pH 7.4); (b) calibration curve for anodic peak current (I_{pa}) *versus* the nitrite concentration (SD $\leq$ 1.17 for 5 repeated whole cycles). Inset: Expanded scale in the 0–50 µM range of NaNO$_2$.

anions by MoS$_2$, it has been reported that some Mo^{6+}, obtained upon applying a potential of about 1 V, may be responsible for the following reaction:[22]

$$\text{Mo}^{6+} + \text{NO}_2^- + \text{H}_2\text{O} \rightarrow \text{Mo}^{4+} + \text{NO}_3^- + 2\text{H}^+$$

In this context, we detected $\sim$5% of MoO$_3$ (Mo^{6+}) in our composite (see above the Raman and XPS data); therefore, the sensing activity of our material was intrinsically possessed. Note that our present study is not really concerned with identifying the nature of compensating defects such as cation vacancies, interstitial sulfur, more complex defect clusters, or defects at the grain boundaries.[54,55]

Concerning the specific role of the 1T and 2H MoS$_2$ phases for the electrochemical sensing of nitrites, the metallic 1T-MoS$_2$ (highly active at both edges and basal planes) represents the most active phase for electrochemical sensing, since possesses excellent electrical conductivity, while the semiconducting 2H-MoS$_2$ phase (that has only active edges) is more stable. Therefore, the synergic contribution of both 1T (metallic) and 2H (higher stable) phases are crucial factors in the development of sensible and stable electrochemical sensors.[56,57]

The repeatability of the MoS$_2$/SPCE sensing ability for NO$_2^-$ was demonstrated by replicating five times the analyses at a

11218 | *J. Mater. Chem. C*, 2025, **13**, 11214–11222

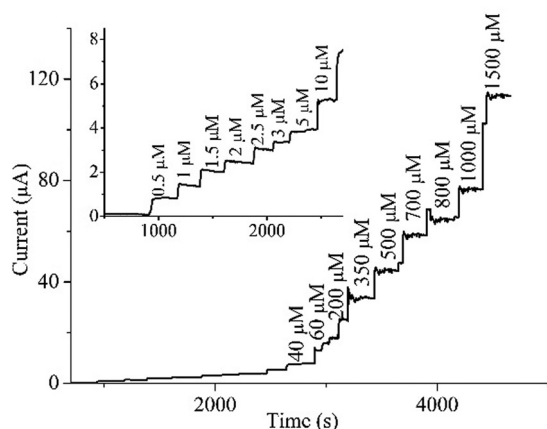This journal is © The Royal Society of Chemistry 2025

Fig. 7 Current–time response of the MoS$_2$/SPCE electrode upon successive additions of nitrite to the 0.1 M PBS electrolyte at 0.6 V; the inset shows the response with 0–10 μM of nitrite.

concentration of 20 μM (Fig. S6a, ESI†); the calculated standard deviation was 0.78. Chronoamperometry was also applied to better assess the NO$_2^-$ sensing limit of MoS$_2$/SPCE using a constant applied potential (0.6 V *vs.* Ag/AgCl). Fig. 7 shows the current response upon changing the nitrite concentration. The increase in oxidation current reaches a plateau in 2 s upon increasing the [NO$_2^-$], up to the tested 1500 μM concentration. The corresponding calibration curve, shown in Fig. 8, shows the linear fit of the current *vs.* the nitrite μM concentration, which yields a sensitivity of 259 μA μM^{-1} cm^{-2} and a LOD value of 0.085 μM.

To assess the ability of the MoS$_2$/SPCE sensor to detect nitrite anions in real samples (without the use of PBS), we performed DPV measurements on commercial nitrite-free bottled water, before and after adding 1, 2, and 20 μM of NO$_2^-$ (Fig. S6b, ESI†). The calculated recoveries ranged between 99.3% and 104.4% (Table 1).[58] Such results indicate that the MoS$_2$/SPCE sensor selectively detects nitrite anions even in the presence of other potential interfering species (those stated by the Fontenoce factory: Cl$^-$, Ca^{2+}, Mg^{2+}, K$^+$, SO$_4^{2-}$, F$^-$, SiO$_2$, HCO$_3^-$, Na$^+$, and NO$_3^-$).[59] Furthermore, we investigated the
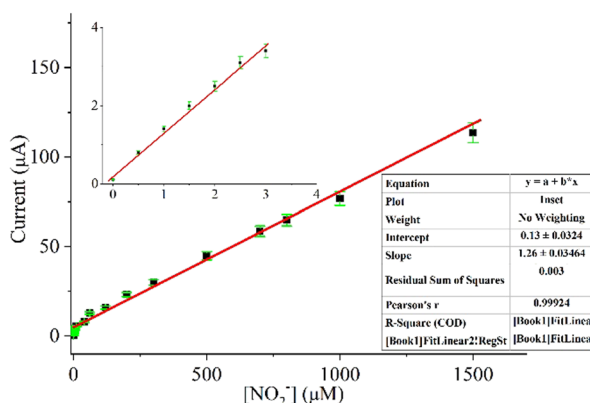

Fig. 8 Calibration line for detecting and quantifying nitrite. The inset shows the calibration line for 0–3 μM of nitrite.

Table 1 Determination of NO$_2^-$ ions added to a commercial bottled water sample (Fontenoce)[58]

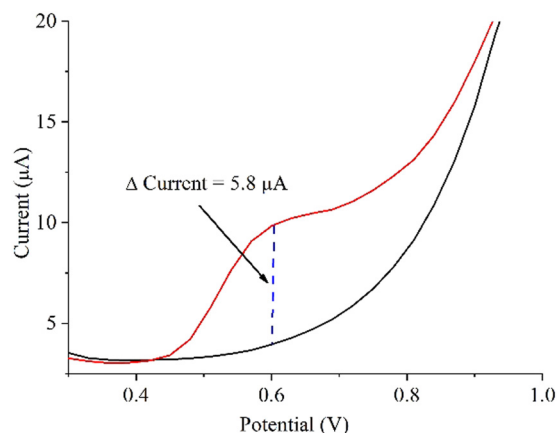| Sensor	[NO$_2^-$] (μM)	ΔCurrent (μA)	Recovery (%)
MoS$_2$/SPCE	1 in 0.1 M PBS	1.47	100
''	2 in 0.1 M PBS	2.56	100
''	20 in 0.1 M PBS	5.54	100
''	1 in bottled water	1.46	99.3
''	2 in bottled water	2.67	104.4
''	20 in bottled water	5.57	100.5

Fig. 9 DPV analyses to determine the nitrite in an Italian sausage (bresaola).

nitrite concentration by DPV in an Italian sausage (bresaola) (Fig. 9). The measured current variation at the exact expected nitrite oxidation potential (0.6 V), using the already optimized potential step, potential pulse, time pulse, and scan rate (see Experimental), was 5.8 μA. Using the calibration line shown in Fig. 6b, and considering the performed dilution (see Experimental), we obtained 72.8 mg nitrite per kg sausage. This value is very close to the limit indicated by European legislation (80 mg kg^{-1}) for this kind of food product.

In addition, to further investigate the ability of our MoS$_2$/SPCE sensor to detect nitrite anions in real samples, we measured the DPV in water containing single interferents (100 μM each), as shown in Fig. 10. The results further show the selectivity of the material.

Furthermore, the MoS$_2$/SPCE sensor exhibits good stability that extends at least six months after its initial use (Fig. S6c, ESI†).

The response of the MoS$_2$/SPCE sensor to 200 μM nitrite at different pH values (5.0–8.0) is shown in Fig. S7 (ESI†) and indicates a small shift toward lower oxidation potentials (0.67–0.53 V) as the pH increases from 5.0 to 8.0. Fig. S8 (ESI†) shows virtually no change in current or potential as the ionic strength increases from 0.1 to 0.2 M.

Electrochemical and optical methods are often used for nitrite sensing in water and food.[21,60–69] Catalytic and electrocatalytic nitrite determination in aqueous solution have been reported as well.[70,71] Therefore, the already reported LODs for nitrite sensing (Table 2) seem to span a large range, with values
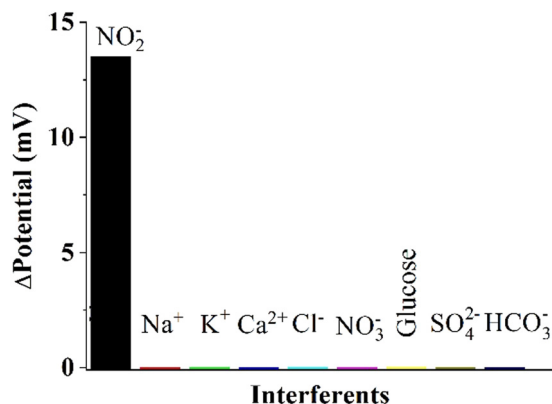
This journal is © The Royal Society of Chemistry 2025

J. Mater. Chem. C, 2025, **13**, 11214–11222 | **11219**

Fig. 10 The histogram shows the response of the MoS$_2$/SPCE toward possible interferents (100 μM each) and nitrite in water.

Table 2 Comparison of the nitrite detection performances of the present MoS$_2$/SPCE and some reported sensing systems

Electrode modifier	Method	Linear range (μM)	LOD (μM)	Ref.
Ag/HNTs/MoS$_2$/CPE	CA	2–425	0.7	23
Ag/H-C$_3$N$_4$/CC-1	CA	5–1000	0.9	80
Au/NiO/rGO/SPCE	DPV	1–500	0.2	81
Pd–Cu–Mo$_2$C/GCE	CA	5–165	0.35	63
Ni/MoS$_2$/GCE	DPV	20–1000	2.74	82
AuNPs/GCE	DPV	10–3800	2.4	83
NBC180/SPCE	DPV	1–1400	2.08	16
3DMoS$_2$/2DC$_3$N$_4$/GCE	DPV	0.1–1100	0.065	21
CoBIM/CTAB	ECL	1–1500	0.67	84
MoS$_2$/SPCE	CA	1–1000	0.085	This work

as low as ∼0.065 μM; however, often the sensing platforms required multi-step syntheses or rather complex apparatuses other than the one we reported.[72–79]

It turns out that the LOD value obtained with our rather simple sensor (0.085 μM, see the present chronoamperometry results) is within the state of-the art.

Conclusions

We synthesized a composite material having a graphitic MoS$_2$/C composition and a nanoribbon morphology well-tailored for the current sensing applications.[67] The MoS$_2$/SPCE sensor was found to be highly sensitive to nitrite concentrations, showing a sensitivity of 4.993 μA μM^{-1} cm^{-2} and a LOD value of 0.085 μM. The sensor is selective and can be reset by simply washing in distilled water. The overall performance is comparable or even better than that of the previously reported nitrite sensors.

Author contributions

A. Gulino: conceptualization, device design, writing, editing, and funding; F. Florio: calibration analysis, device design, experimental and statistical analyses, and writing; A. Ferlazzo: calibration analysis, device design, experimental and statistical analyses, and writing; S. Bonforte: experimental analyses;

G. Nicotra: experimental analyses, writing; G. Neri: experimental and statistical analyses; M. E. V. D. Boom: conceptualization, writing, and editing; I. Pinkas: experimental analyses.

Data availability

The data supporting this article have been included in the main text and as part of the ESI.†

Conflicts of interest

There are no conflicts to declare.

Acknowledgements

Notes and references

1 M. Chhowalla, H. S. Shin, G. Eda, L.-J. Li, K. P. Loh and H. Zhang, *Nat. Chem.*, 2013, **5**, 263–275.

2 J. L. Musfeldt, Y. Iwasa and R. Tenne, *Phys. Today*, 2020, **73**, 42–48.

3 S. Manzeli, D. Ovchinnikov, D. Pasquier, O. V. Yazyev and A. Kis, *Nat. Rev. Mater.*, 2017, **2**, 17033.

4 D. Kozawa, P. Liu, Y. Zeng, V. B. Koman, M. Kuehne and M. S. Strano, *Nano Lett.*, 2020, **20**, 3067–3078.

5 G. Eda, H. Yamaguchi, D. Voiry, T. Fujita, M. Chen and M. Chhowalla, *Nano Lett.*, 2011, **11**, 5111–5116.

6 D. S. Schulman, D. May-Rawding, F. Zhang, D. Buzzell, N. Alem and S. Das, *ACS Appl. Mater. Interfaces*, 2018, **10**, 4285–4294.

7 Y. Dong, M.-M. Yang, M. Yoshii, S. Matsuoka, S. Kitamura, T. Hasegawa, N. Ogawa, T. Morimoto, T. Ideue and Y. Iwasa, *Nat. Nanotechnol.*, 2023, **18**, 36–41.

8 P. S. Kiran, K. V. Kumar, N. Pandit, S. Indupuri, R. Kumar, V. V. Wagh, A. Islam and A. K. Keshri, *Adv. Funct. Mater.*, 2024, **34**, 2316266.

9 H. Wang, C. Li, P. Fang, Z. Zhang and J. Z. Zhang, *Chem. Soc. Rev.*, 2018, **47**, 6101–6127.

10 L. Li, Q. Wang, F. Wu, Q. Xu, J. Tian, Z. Huang, Q. Wang, X. Zhao, Q. Zhang, Q. Fan, X. Li, Y. Peng, Y. Zhang, K. Ji, A. Zhi, H. Sun, M. Zhu, J. Zhu, N. Lu, Y. Lu, S. Wang, X. Bai, Y. Xu, W. Yang and G. Zhang, *Nat. Commun.*, 2024, **15**, 1825.

11 A. Dodda, D. Jayachandran, A. Pannone, N. Trainor, S. P. Stepanoff, M. A. Steves, S. S. Radhakrishnan, S. Bachu, C. W. Ordonez, J. R. Shallenberger, J. M. Redwing,

11220 | *J. Mater. Chem. C*, 2025, **13**, 11214–11222

This journal is © The Royal Society of Chemistry 2025

K. L. Knappenberger, D. E. Wolfe and S. Das, *Nat. Mater.*, 2022, **21**, 1379–1387.

12 V. D. Dang, R. Putikam, M. C. Lin and K. H. Wei, *Small*, 2024, **20**, 2305220.

13 T. X. Huang, X. Cong, S. S. Wu, J. B. Wu, Y. F. Bao, M. F. Cao, L. Wu, M. L. Lin, X. Wang, P. H. Tan and B. Ren, *Nat. Catal.*, 2024, **7**, 646–654.

14 J. Sengupta and C. M. Hussain, *TrAC, Trends Anal. Chem.*, 2024, 117742.

15 D. Zhang, M. Li, Y. Yang, H. Yu, F. Xiao, C. Mao, J. Huang, Y. Yu, Y. Wang, B. Wu, C. Wang, L. Shu, Z. He and Q. Yan, *Water Res.*, 2022, **220**, 118637.

16 A. Ferlazzo, V. Bressi, C. Espro, D. Iannazzo, E. Piperopoulos and G. Neri, *J. Electroanal. Chem.*, 2023, **928**, 117071.

17 N. Ibrahim, M. A. Hefnawy, S. A. Fadlallah and S. S. Medany, *Food Chem.*, 2024, 140962.

18 C. N. Carroll, J. J. Naleway, M. M. Haley and D. W. Johnson, *Chem. Soc. Rev.*, 2010, **39**, 3875–3888.

19 I. H. Abidi, S. P. Giridhar, J. O. Tollerud, J. Limb, M. Waqar, A. Mazumder, E. L. H. Mayes, B. J. Murdoch, C. Xu, A. Bhoriya, A. Ranjan, T. Ahmed, Y. Li, J. A. Davis, C. L. Bentley, S. P. Russo, E. Della Gaspera and S. Walia, *Adv. Funct. Mater.*, 2024, **34**, 2402402.

20 J. F. Tan, A. Anastasi and S. Chandra, *Curr. Opin. Electrochem.*, 2022, **32**, 100926.

21 L. Wang, Z. Fan, F. Yue, S. Zhang, S. Qin, C. Luo, L. Pang, J. Zhao, J. Du, B. Jin and H. Zhang, *Food Chem.*, 2024, **430**, 137027.

22 H. L. Zou, L. Y. Qin, H. Q. Luo, B. L. Li and N. B. Li, *Sens. Actuators, B*, 2021, **337**, 129812.

23 M. Ghanei-Motlagh and M. A. Taher, *Biosens. Bioelectron.*, 2018, **109**, 279–285.

24 N. Abid, A. M. Khan, S. Shujait, K. Chaudhary, M. Ikram, M. Imran, J. Haider, M. Khan, Q. Khan and M. Maqbool, *Adv. Colloid Interface Sci.*, 2022, **300**, 102597.

25 S. H. Choi, S. J. Yun, Y. S. Won, C. S. Oh, S. M. Kim, K. K. Kim and Y. H. Lee, *Nat. Commun.*, 2022, **13**, 1484.

26 A. Gulino, G. G. Condorelli and I. Fragalà, *J. Mater. Chem.*, 1996, **6**, 1335–1338.

27 D. Briggs and J. T. Grant, *Surface Analysis by Auger and X-Ray Photoelectron Spectroscopy*, IMP, Chichester, UK, 2003.

28 A. Gulino, *Anal. Bioanal. Chem.*, 2013, **405**, 1479–1495.

29 G. Greczynski and L. Hultman, *Angew. Chem., Int. Ed.*, 2020, **59**, 5002–5006.

30 O. L. Krivanek, N. Dellby, M. F. Murfitt, M. F. Chisholm, T. J. Pennycook, K. Suenaga and V. Nicolosi, *Ultramicroscopy*, 2010, **110**, 935–945.

31 A. Ferlazzo, A. Gulino and G. Neri, *Environ. Sci.: Adv.*, 2024, **3**, 1392–1399.

32 P. Phalswal, P. K. Khanna, H.-G. Rubahn and Y. K. Mishra, *Mater. Adv.*, 2022, **3**, 5672–5697.

33 R. C. Mehrotra, R. Bohra and D. P. Gaur, *Metal β-Diketonates and Allied Derivatives*, Academic Press, London, 1978.

34 A. Jawaid, D. Nepal, K. Park, M. Jespersen, A. Qualley, P. Mirau, L. F. Drummy and R. A. Vaia, *Chem. Mater.*, 2016, **28**, 337–348.

35 H. Ma, S. Ben, Z. Shen, X. Zhang, C. Wu, S. Liao and F. An, *Appl. Surf. Sci.*, 2020, **512**, 145588.

36 J. Strachan, A. F. Masters and T. Maschmeyer, *J. Mater. Chem. A*, 2021, **9**, 9451–9461.

37 Y. Zhang, J. Li, X. Li, L. Shan, W. Zhao, J. Wang, Q. Gao, Z. Cai, C. Zhou, B. Han, K. Amine and R. Sun, *Nano Lett.*, 2024, **24**, 3331–3338.

38 J. Bai, B. Zhao, J. Zhou, J. Si, Z. Fang, K. Li, H. Ma, J. Dai, X. Zhu and Y. Sun, *Small*, 2019, **15**, 1805420.

39 G. Mestl, P. Ruiz, B. Delmon and H. Knozinger, *J. Phys. Chem.*, 1994, **98**, 11269–11275.

40 M. Sarkar, R. Hossain and V. Sahajwalla, *Carbon*, 2023, **213**, 118274.

41 H. Cao, Z. Bai, Y. Li, Z. Xiao, X. Zhang and G. Li, *ACS Sustainable Chem. Eng.*, 2020, **8**, 7343–7352.

42 D. Scirè, R. Macaluso, M. Mosca, S. Mirabella, A. Gulino, O. Isabella, M. Zeman and I. Crupi, *Solid-State Electron.*, 2021, **185**, 108135.

43 A. Gulino, S. Parker, F. H. Jones and R. G. Egdell, *J. Chem. Soc., Faraday Trans.*, 1996, **92**, 2137–2141.

44 S. Wang, D. Zhang, B. Li, C. Zhang, Z. Du, H. Yin, X. Bi and S. Yang, *Adv. Energy Mater.*, 2018, **8**, 1801345.

45 D. Tsikritzis, N. Tsud, T. Skála and L. Sygellou, *Appl. Surf. Sci.*, 2022, **599**, 153896.

46 Y. Wang, W. Zhai, Y. Ren, Q. Zhang, Y. Yao, S. Li, Q. Yang, X. Zhou, Z. Li, B. Chi, J. Liang, Z. He, L. Gu and H. Zhang, *Adv. Mater.*, 2024, **36**, 2307269.

47 X. Guan, L. Zhao, P. Zhang, J. Liu, X. Song and L. Gao, *Mater. Today Energy*, 2020, **16**, 100379.

48 J. Ekspong, R. Sandström, L. P. Rajukumar, M. Terrones, T. Wågberg and E. Gracia-Espino, *Adv. Funct. Mater.*, 2018, **28**, 1802744.

49 W. Han, J. Wang, X. Li, L. Zhou, Y. Yang, M. Tang and H. Ge, *Catal. Commun.*, 2019, **124**, 86–91.

50 Y.-H. Choi, J. Cho, A. M. Lunsford, M. Al-Hashimi, L. Fang and S. Banerjee, *J. Mater. Chem. A*, 2017, **5**, 5129–5141.

51 L. Fei, S. Lei, W.-B. Zhang, W. Lu, Z. Lin, C. H. Lam, Y. Chai and Y. Wang, *Nat. Commun.*, 2016, **7**, 12206.

52 C. M. Cardona, W. Li, A. E. Kaifer, D. Stockdale and G. C. Bazan, *Adv. Mater.*, 2011, **23**, 2367–2371.

53 K. Abid, A. Ferlazzo and G. Neri, *FlatChem*, 2024, **46**, 100673.

54 S. Millesi, M. R. Catalano, G. Impellizzeri, I. Crupi, G. Malandrino, F. Priolo and A. Gulino, *Mater. Sci. Semicond. Process.*, 2017, **69**, 32–35.

55 A. Gulino, A. E. Taverner, S. Warren, P. Harris and R. G. Egdell, *Surf. Sci.*, 1994, **315**, 351–361.

56 S. Ren, W. Cui, Y. Liu, S. Cheng, Q. Wang, R. Feng and Z. Zheng, *Sens. Actuators, A*, 2022, **345**, 113772.

57 S. Ren, R. Feng, S. Cheng, L. Huang, Q. Wang and Z. Zheng, *Microchem. J.*, 2022, **175**, 107129.

58 J. H. Zhang, Q. Shen and Y. G. Zhou, *ACS Sens.*, 2021, **6**, 2320–2329.

59 Chemical and physico-chemical analyses stated for the Fontenoce bottled water: Specific electrical conductivity measured at 20 °C = 147 μS cm^{-1}, source temperature 9.3 °C, pH at

This journal is © The Royal Society of Chemistry 2025

J. Mater. Chem. C, 2025, **13**, 11214–11222 | **11221**

the source 7.69, fixed residue at 180 $^{\circ}$C = 103.4 mg L^{-1}, NO$_2^-$ absent, Ca^{2+} 16.2 mg L^{-1}, Mg^{2+} 5.9 mg L^{-1}, Na$^+$ 7.2 mg L^{-1}, K$^+$ 1.6 mg L^{-1}, HCO$_3^-$ 75.3 mg L^{-1}, SO$_4^{2-}$ 8.9 mg L^{-1}, Cl$^-$ 6.9 mg L^{-1}, NO$_3^-$ 1.7 mg L^{-1}, F$^-$ 0.13 mg L^{-1}, SiO$_2$ 16.9 mg L^{-1}.

60 D. Thatikayala and B. Min, *Biosens. Bioelectron.*, 2023, **241**, 115659.

61 L. Britschgi, K. Villez, P. Schrems and K. M. Udert, *Water Res. X*, 2020, **9**, 100055.

62 S. Velmurugan, S. Palanisamy and T. C.-K. Yang, *Sens. Actuators, B*, 2020, **316**, 128106.

63 A. T. E. Vilian, R. Umapathi, S.-K. Hwang, Y. S. Huh and Y.-K. Han, *J. Hazard. Mater.*, 2021, **408**, 124914.

64 W. Zhu, Y. Zhang, J. Gong, Y. Ma, J. Sun, T. Li and J. Wang, *ACS Sens.*, 2019, **4**, 2980–2987.

65 T. Zhang, Y. Liu, J. Li, W. Ren and X. Dou, *Sens. Actuators, B*, 2023, **379**, 133261.

66 L. Singh and N. Ranjan, *J. Am. Chem. Soc.*, 2023, **145**, 2745–2749.

67 J. Zhang, T. Hu, B. Xiong, X. Zheng, R. Wang, P. Zhu, J. Chen, T. Cong, Y. Li and X. Wang, *Chem. Eng. J.*, 2023, **475**, 146311.

68 Z. Ma, J. Li, X. Hu, Z. Cai and X. Dou, *Adv. Sci.*, 2020, **7**, 2002991.

69 L. Tan, C. Xie, Q. Yang, K. Luo and L. Zhou, *Food Chem.*, 2023, **405**, 134949.

70 V. C. A. Ficca, C. Santoro, E. Marsili, W. Da Silva Freitas and A. Serov, *Electrochim. Acta*, 2022, **402**, 139514.

71 A. Shaikh, B. K. Singh and S. Parida, *Mater. Chem. Phys.*, 2019, **235**, 121744.

72 Y. Dong, F. Liu, S. Liu, S. Feng and S. Peng, *ACS Appl. Nano Mater.*, 2024, **7**, 16620–16629.

73 T. Zhe, F. Li, M. Liu, K. Ma, Q. Luo and W. Li, *Chem. Eng. J.*, 2024, **488**, 150942.

74 M. J. Askari, J. D. Kallick and C. C. L. McCrory, *J. Am. Chem. Soc.*, 2024, **146**, 7439–7455.

75 L. Bai, F. Franco, J. Timoshenko, C. Rettenmaier, F. Scholten, H. S. Jeon, A. Yoon, M. Rüscher, A. Herzog, F. T. Haase, S. Kühl, S. W. Chee, A. Bergmann and R. C. Beatriz, *J. Am. Chem. Soc.*, 2024, **146**, 9665–9678.

76 M. Ghosh, S. E. Braley, R. Ezhov, H. Worster, J. A. Valdez-Moreira, Y. Losovyj, E. Jakubikova, Y. N. Pushkar and J. M. Smith, *J. Am. Chem. Soc.*, 2022, **144**, 17824–17831.

77 P. Huang, Y. Yan, P. Martinho Ricardo, L. Lefferts, B. Wang and J. F. Albanese, *J. Am. Chem. Soc.*, 2024, **4**, 2656–2665.

78 P. Li, R. Li, Y. Liu, M. Xie, Z. Jin and G. Yu, *J. Am. Chem. Soc.*, 2023, **145**, 6471–6479.

79 S. K. Kailasa, M. R. Patel, J. R. Koduru and T. J. Park, *Chem. Rev.*, 2024, **501**, 215595.

80 Y. Shen, C. Ma, S. Zhang, P. Li, W. Zhu, X. Zhang, J. Gao, H. Song, D. Chen, D. Pang and A. Li, *Sci. Total Environ.*, 2020, **742**, 140622.

81 K. Xu, Q. Chen, Y. Zhao, C. Ge, S. Lin and J. Liao, *Sens. Actuators, B*, 2020, **319**, 128221.

82 Y. Yang, J. Zhang, Y. W. Li, Q. Shan and W. Wu, *Colloids Surf., A*, 2021, **625**, 126865.

83 H. Shi, L. Fu, F. Chen, S. Zhao and G. Lai, *Environ. Res.*, 2022, **209**, 112747.

84 Y. X. Dai, Y. X. Li, X. J. Zhang, R. S. Marks, S. Cosnier and D. Shan, *ACS Sens.*, 2024, **9**, 337–343.

11222 | *J. Mater. Chem. C*, 2025, **13**, 11214–11222

This journal is © The Royal Society of Chemistry 2025